ACS APPLIED MATERIALS & INTERFACES

www.acsami.org Research Article

Porous PDMS–ZnO Wearable Gas Sensor for Acetone Biomarker Detection and Breath Analysis

Yanru Chen, Yixin Liu, Jiaqi Liu, Yuzhen Li, Yuhan Liu, Wenjie Zhang, Liuyang Han, Dongkai Wang, Shuhong Cao, Hanxiao Liu, Qisen Xie, Xiaohao Wang, and Min Zhang*

Cite This: *ACS Appl. Mater. Interfaces* 2024, 16, 62436–62445 Read Online

ACCESS | Metrics & More | Article Recommendations | Supporting Information

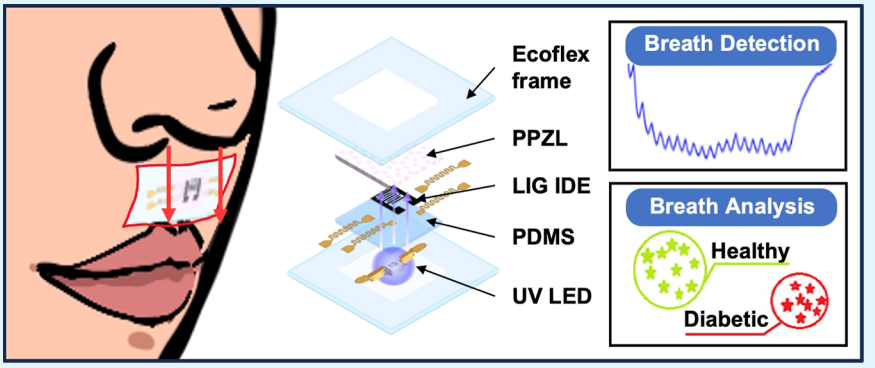

ABSTRACT: In response to the growing demand for global health monitoring, we report a nonintrusive health detection method using a compact, conformal wearable ultraviolet (UV)-assisted gas-sensing system based on an intrinsically flexible porous polydimethylsiloxane (PDMS)-zinc oxide (ZnO) composite layer (PPZL) for the breath acetone (BrAce) detection and breath event analysis. The enhanced acetone response is attributed to the synergistic effect of UV irradiation and the high surface area of the porous structure, which also improves the mechanical robustness. The UV-assisted wearable sensor reliably detects acetone concentrations ranging from 1 to 100 ppm at room temperature under 4.05 mW/cm^2 UV intensity, even under mechanical strains such as a bending radius of 5 mm and 60% tensile strain. It accurately analyzes different breathing patterns (12–20 breaths per minute) and BrAce concentrations, maintaining a stable performance over 20 days with less than 5% signal degradation. The sensor exhibits response and recovery times of average 110–150 and 130–180 s, respectively, and maintains a consistent 3 ppm BrAce response under varying humidity levels up to 70% relative humidity, ensuring accurate detection of BrAce concentrations during real-world breath tests. Additionally, the sensor targets only specific gases, and the sensor's selectivity is not a key concern. This flexible acetone gas sensor offers a portable solution for health management and a fabrication method for designing flexible metal oxide materials.

KEYWORDS: *porous PDMS–ZnO composite, ultraviolet-assisted, conformal gas sensor, breath acetone detection, breath event analysis*

1. INTRODUCTION

With the increasing prevalence of chronic diseases like diabetes mellitus[1−3] and sleep apnea-hypopnea syndrome (SAHS),[4,5] noninvasive breath analysis[6] for biomarkers[7,8] such as acetone[9,10] and the monitoring of breathing events have become crucial for comprehensive health monitoring and personal health management. However, current breath analyzer technologies[9,10] are often bulky and uncomfortable. To date, wearable gas sensors, such as smart masks detecting hydrogen peroxide through differential electrochemical measurement methods,[11] those measuring respiratory status via surface pressure changes,[12] or nylon fiber sensors using zinc oxide (ZnO) quantum dot-doped reduced-graphene oxide for nitrogen dioxide detection,[13] are generally nonconformal and lack mechanical robustness, limiting their comfort and long-term usability.

Metal oxide (MOX) materials are considered among the most promising candidates because of their remarkable sensitivity, stability, and versatility in detecting various gases.[14,15] Among the different types of MOXs, ZnO, due to its high electron mobility,[16] morphology tunability,[17] and excellent chemical stability,[18] is particularly suitable for acetone

Received: September 21, 2024
Revised: October 19, 2024
Accepted: October 23, 2024
Published: October 31, 2024

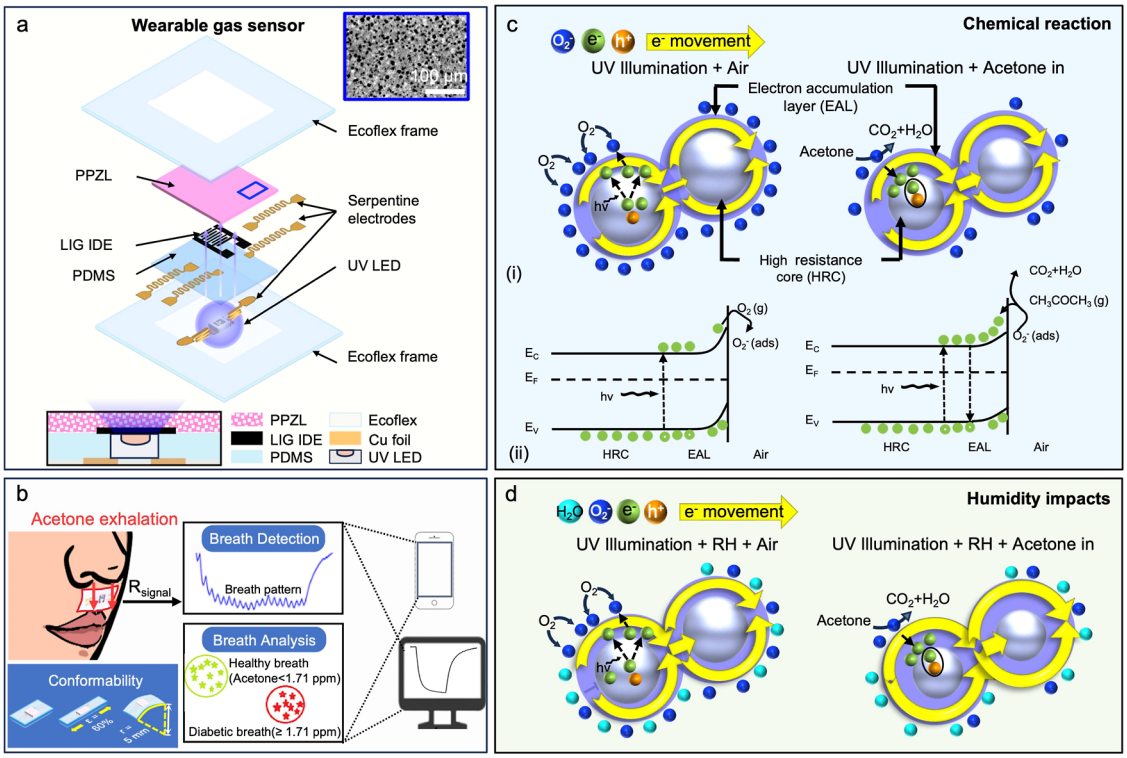

Figure 1. Structure and gas-sensing mechanism of the wearable acetone gas sensor. (a) Schematic diagram of the wearable gas sensor showing its layered structure, and the inset picture shows a microscopic image of the PPZL surface, indicating its porous nature. (b) Illustration of the breath detection and analysis system using the wearable sensor. The sensor detects acetone in exhaled breath, indicated by changes in resistance. (c) Mechanism of acetone gas sensing under UV illumination. (i) Sensor operates by facilitating electron movement within the electron accumulation layer (EAL) when exposed to UV light in the presence of air. Upon acetone exposure, a chemical reaction occurs, converting acetone to CO_2 and H_2O, altering the electrical resistance. (ii) Energy band diagrams illustrating the electron transitions and the formation of O_2^- on the sensor surface. (d) Impact of RH on the gas-sensing performance. The presence of water molecules (H_2O) in the air affects the adsorption and reaction processes on the sensor surface. UV illumination in humid air conditions still facilitates the electron movement and reaction with acetone.

sensing. For example, ZnO/$LaFeO_3$ nanocomposite sensors[19] have demonstrated exceptional sensitivity, with a response of approximately 208.7 at 100 ppm acetone at an optimal operating temperature of 340 °C—39 times higher than pure ZnO sensors—attributed to p−n heterojunction formation that enhances charge carrier dynamics. Similarly, aluminum-doped ZnO thin-film sensors[20] show optimal acetone-sensing at 300 °C, with a maximum response of 13.41 at 10 ppm and effective detection down to 2 ppm. Furthermore, 2D-material graphene-like ZnO/graphene oxide (GO) nanosheets,[21] synthesized via a wet-chemical method and calcining, provide high response and rapid recovery (94 s/4 s for 100 ppm acetone vapor), with an extremely selective acetone vapor sensor were reached by choosing 525 °C. Additionally, 1D ZnO quantum dots[22] capped with 3-aminopropyl triethoxysilane offer a wide linear response range (0.1−18 mM), low detection limit (42 μM), and excellent selectivity. ZnO is also a wide band gap semiconductor (approximately 3.37 eV) with a very high photoconductivity, particularly in the ultraviolet (UV) range. Jaisutti et al.[23] leveraged the photocatalytic activity of Na-doped p-type ZnO nanoflowers to develop a room-temperature acetone gas sensor, which exhibited high gas response and rapid response times (83 s/63 s) to 100 ppm acetone gas under UV light intensity of 5 mW/cm^2, achieving detection of acetone down to 0.2 ppm at room temperature. Similarly, Zhang et al.[24] synthesized Na/reduced graphene oxide (rGO) heterojunctions, which could detect acetone concentrations ranging from 5 to 200 ppm at room temperature, with response/recovery times of 80 s/135 s for 100 ppm acetone. Despite their promising attributes, gas sensors composited of ZnO and related materials often require high operating temperatures and rigid substrates, which limit their application in wearable devices for continuous use in the human body.

This study addresses these challenges by developing a novel thermal phase separation method to embed ZnO nanoparticles (ZnO NPs) into a flexible polydimethylsiloxane (PDMS) substrate, creating an intrinsically flexible porous PDMS−ZnO NP composite layer (PPZL). This composite layer is then integrated with a UV LED and flexible electrodes into a fully flexible, conformal sensor for accurate room-temperature BrAce detection and breath event analysis. The manufacturing parameters and UV light irradiation affecting the sensor's performance were optimized through experimental and theoretical approaches. The sensor can detect acetone gas concentrations ranging from 1 to 100 ppm at room temperature using 4.05 mW/cm^2 UV light, and it remains unaffected by high-humidity environments [30%−73% relative humidity (RH)]. This range encompasses typical BrAce concentrations,[9,25,26] where healthy individuals generally exhibit undetectable levels between 0.22 and 0.80 ppm, while diabetic patients often present levels exceeding 1.76 ppm. The gas sensitivity performance was investigated under different tensile (maximum strain: 60%) and bending (minimum radius: 5 mm) conditions to ensure that skin strain of ∼30% during wear does not affect gas response. The device incorporates an

https://doi.org/10.1021/acsami.4c16209
ACS Appl. Mater. Interfaces 2024, 16, 62436−62445

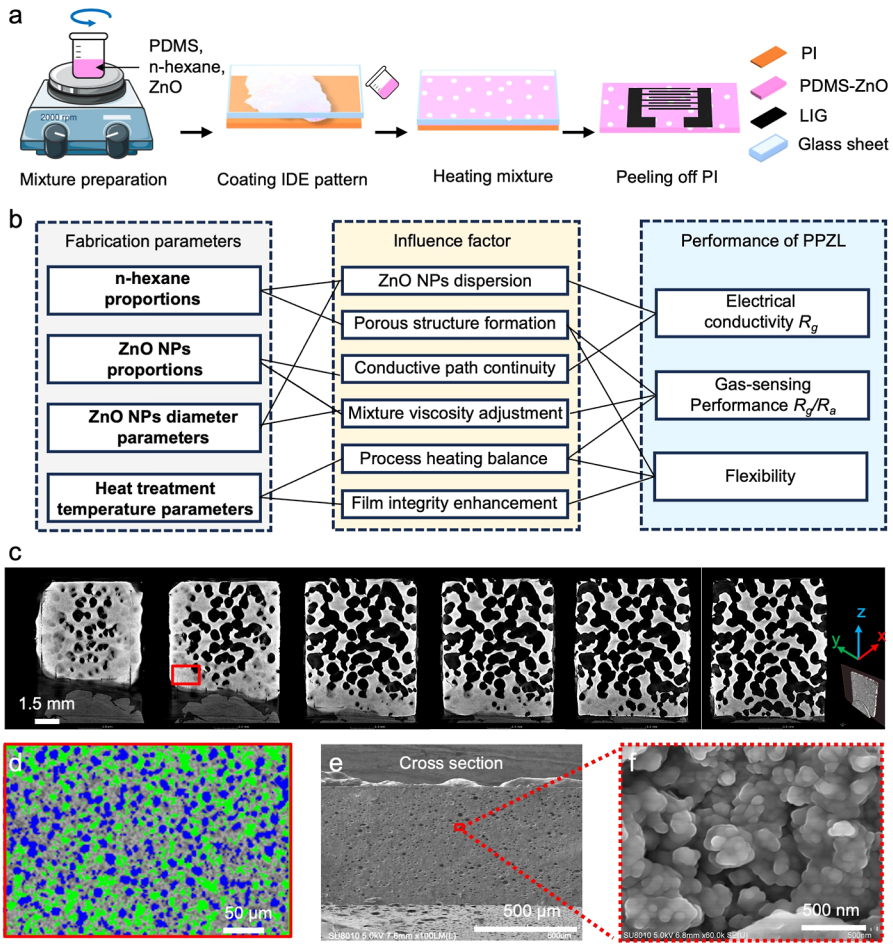

Figure 2. Fabrication process and morphology of PPZL. (a) PPZL fabrication process. (b) Flowchart of the fabrication parameters, influence factors, and performance outcomes of PPZL. (c) PPZL-segmented computed tomography (CT) data. (d) Enlarged view of the segmented CT data, highlighting the microholes (blue) and ZnO NPs (green). (e) Cross-sectional scanning electron microscopy (SEM) data. (f) Enlarged SEM picture of microholes within the PPZL.

ESP32 C3 Bluetooth chip for wireless transmission and is designed for comfortable long-term wear under the nose. The ability to detect various breathing patterns was demonstrated in human tests, while consistent responsiveness to 3 ppm of BrAce was confirmed across simulated conditions and varied high-humidity environments, ensuring stable acetone sensitivity during breath analysis. In this work, selectivity is not the primary focus due to the nature of exhaled breath analysis. Exhaled breath mainly consists of oxygen, nitrogen, carbon dioxide, water vapor, and trace acetone; the sensor targets only these gases, as the focus is on breath analysis for health management. Since activities like alcohol consumption, which could introduce other gases, are not expected, the sensor's selectivity is not a key concern.

2. RESULTS AND DISCUSSION

2.1. Structure and Gas-Sensing Mechanism of Flexible UV-Assisted Acetone Gas Sensor. In Figure 1a, 3D illustration images of the gas sensor are depicted. The entire stretchable, UV-assisted acetone gas sensor comprises flexible gas-sensing composite PPZL, a UV LED, stretchable laser-induced graphene (LIG) interdigital electrodes (IDEs), stretchable copper serpentine electrodes, and a low-modulus Ecoflex ($E_{\text{Ecoflex}} \approx 60$ kPa) outer frame. UV−vis absorption spectroscopy characterization of ZnO NPs (Figure S1) reveals that the material exhibits its strong light absorption at 365 nm wavelength. During operation, the 365 nm LED emits UV light from the bottom, which is transmitted to the PPZL, initiating its gas-sensing capability. This flexible sensor maintains high linearity in acetone concentration tests even under stretch and strain, enabling wearable breath analysis. Figure 1b demonstrates the application of a wearable room-temperature acetone gas sensor in analyzing exhaled breath. We designed a Bluetooth circuit (Figure S2) for wireless communication that simplifies data processing and transmission, fulfilling the demand for mobile health monitoring. This circuit includes several modules: an ESP 32 C3-based signal transmission module, a power module, a MUX signal selection module, and a sensing module, each aimed at ensuring efficient, stable, and flexible sensor functionality, while also considering user convenience in terms of size. The PCB design for the wearable room-temperature acetone gas sensor measures 2.5 cm in length, 2.1 cm in width, and weighs 2.6 g.

Figure 1c illustrates the acetone-gas-sensing mechanism under UV illumination. Under dark conditions (without UV illumination), oxygen molecules in the air chemisorb on the ZnO surface as oxygen ions (O_2^-) (eq 1). Consequently, the dark conductivity of PPZL remains low.

$$O_2(\text{gas}) + e^- \rightarrow O_2^-(\text{ads}) \quad (1)$$

https://doi.org/10.1021/acsami.4c16209
ACS Appl. Mater. Interfaces 2024, 16, 62436−62445

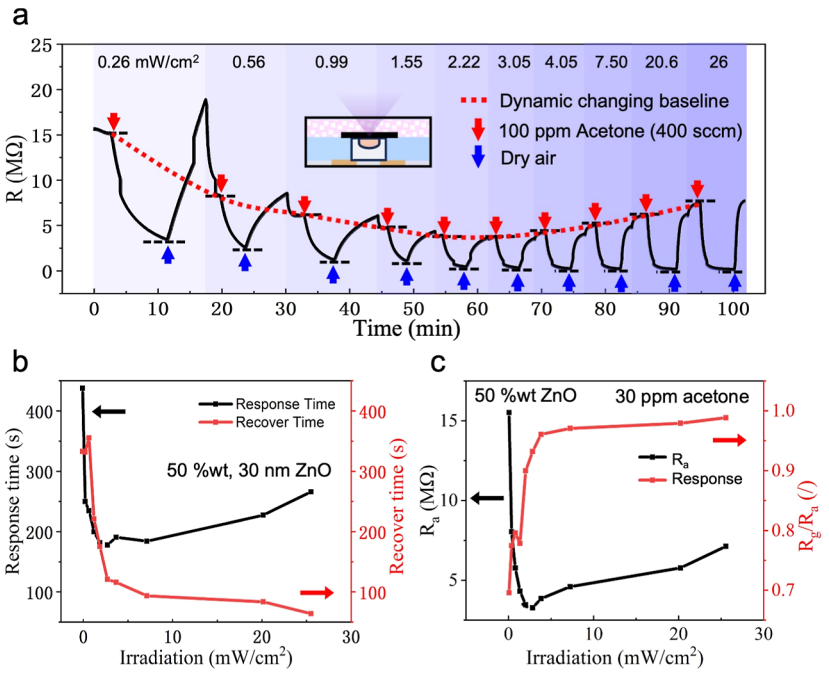

Figure 3. Influence of gas sensor under different UV irradiations (0.26−26 mW/cm^2). (a) Optimized UV irradiation. The red dashed line indicates the dynamic changing baseline, while red and blue arrows mark the introduction of acetone and dry air. (b) Response time and recovery time under different UV irradiations. (c) R_a and response R_g/R_a under different UV irradiations.

When materials are exposed to light with a wavelength of 365 nm, which has an energy of 3.4 eV higher than the band gap energy of 3.37 eV for ZnO,[27] photoexcited electron−hole pairs (EHPs) are generated in ZnO. Electrons are excited to the conduction band, and photoexcited electrons lose their excess energy through phonon emission, transitioning to a thermal equilibrium state. This rapid increase in charge carriers within ZnO leads to an increase in conductivity.

In the presence of light, electrons in the valence band of ZnO become stable thermal equilibrium charge carriers in the conduction band, leading to an increase in the conductivity and a decrease in the resistance. The surface EAL combines with oxygen in the air, resulting in ionization bonding (eq 2).

$$O_2(gas) + e^-(photo) \rightarrow O_2^-(photo) \quad (2)$$

As electrons move from the material's interior to the surrounding environmental gas, the energy bands bend upward, forming a smaller EAL, which increases the material's resistance.

When acetone—a reducing gas—enters the ambient atmosphere around the material—it interacts with O_2^- adsorbed on the ZnO surface. This results in a redox reaction where O_2^- desorb from the material's surface (eq 3), and the electrons they occupied return to the material's surface.

$$CH_3COCH_3(gas) + 4O_2^-(photo) \rightarrow 3CO_2 + 3H_2O + 4e^- \quad (3)$$

The energy bands slightly bend downward, forming a larger EAL, which increases the electrical conductivity and decreases the resistance.

PPZL exhibits high resistance and significant photoconductivity, making it suitable for use at low temperatures. Under light illumination at an irradiation of 5 mW/cm^2, the concentration of photoexcited charge carriers reaches a dynamic steady state after 120 s (Figure S3).

In Figure 1d, the RH impacts under UV illumination are illustrated. In a humid environment, on the same sites as adsorbed O_2^-, H_2O molecules are adsorbed by conversion to the hydroxyl groups.[28] Hydroxyl poisoning can be expressed by

$$H_2O(gas) + O_2^- + S \rightarrow 2(S - OH) + e^- \quad (4)$$

where S is the adsorption site on ZnO. Thus, in humid atmospheres, hydroxyl groups are adsorbed by O_2^-, forming S−OH, and donating electrons to ZnO. Furthermore, the acetone molecule absorbing in high RH environments is affected because it occupies the sites of O_2^-, resulting in changes in the number of active sites that acetone can react with.

2.2. Optimization of PPZL Gas-Sensitive Performance. The conductive gas-sensitive flexible layer PPZL is fabricated through the mechanical blending of PDMS, ZnO NPs, and *n*-hexane into a composite paste by using a thermally induced phase separation method to achieve the porous structure (Figure 2a). The blended paste is poured onto the IDE made of LIG[29] based on a polyimide (PI) substrate via laser direct writing, followed by gradient thermal treatment, and finally peeled from the PI to form an integrated semiconductive PPZL gas-sensitive material. This method not only preserves the material's breathability but also produces an intrinsically flexible composite due to the stretchable PDMS substrate.

PPZL's conductive network is primarily based on the percolation effect[30] and tunneling current effect (Figure S4). Tensile testing[31] revealed that PPZL exhibited good elasticity with Young's modulus of 8.364 MPa and displayed excellent ductility (Figure S5). Figure S6 demonstrates a COMSOL strain simulation exploring how porosity affects the material's mechanical properties. The fabrication process involves various fabrication parameters (Figure 2b) including *n*-hexane proportions, ZnO NP proportions, ZnO NP diameter parameters,[32] and heat treatment temperatures, which will

https://doi.org/10.1021/acsami.4c16209
ACS Appl. Mater. Interfaces 2024, 16, 62436−62445

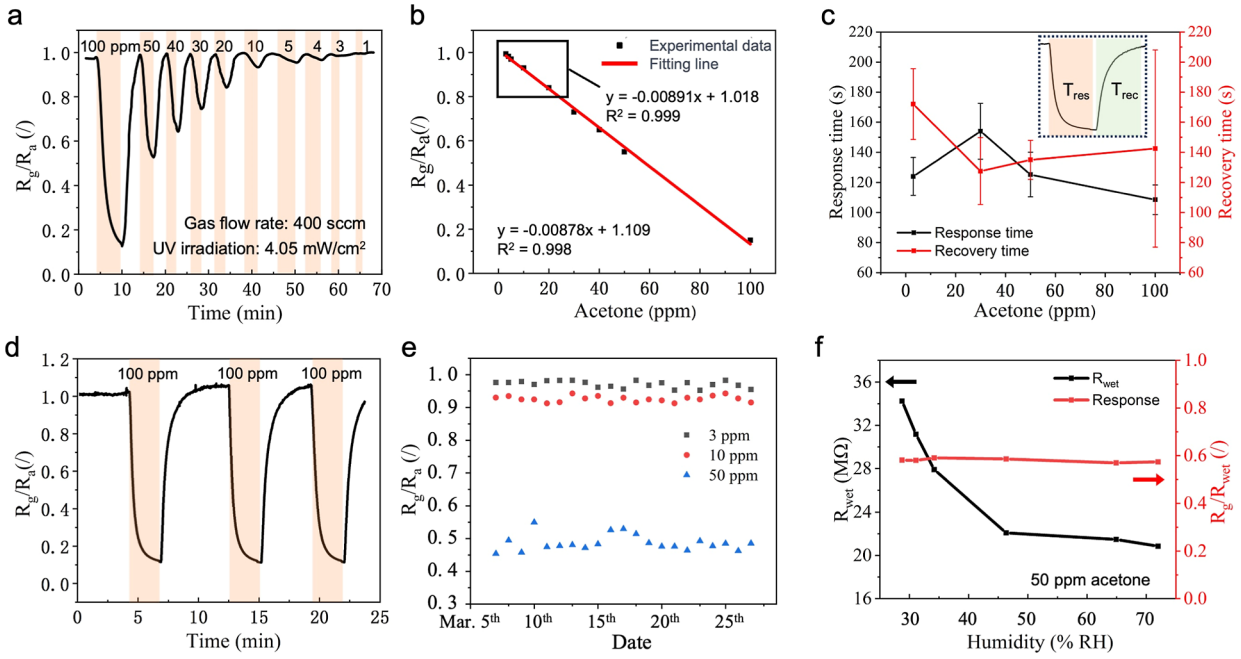

Figure 4. Gas response. (a) Dynamic response of 1−100 ppm acetone. (b) Linearity of 1−100 ppm acetone response and a closer view of the 1−20 ppm response. (c) Response and recovery time for different acetone concentrations with error bars (4 samples). (d) Repetitive test of 100 ppm acetone. (e) Long-term stability test over 20 days at different acetone concentrations (3, 10, and 50 ppm). (f) Gas response under 30%−75% RH at 50 ppm acetone.

impact the performance of PPZL including electrical conductivity, gas-sensing performance, and flexibility (Section S1.3). During fabrication, *n*-hexane facilitates material dilution and promotes the formation of the desired porosity (hole rate, HR > 15%). The material consisting of 30 nm ZnO NPs at a mass ratio of 3:3:4 ZnO/PDMS/*n*-hexane was selected for the fabrication of PPZL.

Figure 2c shows the CT data of optimized PPZL. From segmental images, it is revealed that PPZL contains large pores with diameters of several hundred micrometers that permeate through the material, resulting in high volumetric occupancy and excellent breathability within the material. The average acetone permeability of four PPZL films is measured at 0.857 mg/min·cm^2, with the results detailed in Table S4. The testing setup for PPZL's acetone permeability test is described in Figure S12.

Figure 2d shows a magnified segmented picture of the PPZL internal structure; the smaller pore structure (average diameter ∼4.2 μm) is highlighted in blue, and the distribution of ZnO NPs is highlighted in green. These small pores help to disperse the stress produced by stretching strains, preventing major structural fractures and enhancing the electrical properties of ZnO NPs encapsulated within the PDMS under stress. Figure 2e presents the porous PPZL cross-sectional SEM image, showing a uniform pore size distribution. Figure 2f offers a magnified view inside the pore, revealing 30 nm ZnO NPs encapsulated in PDMS, arranged closely together. The exposed ZnO nanoparticles within the pores come into contact with atmospheric gases. Figure S13 shows detailed SEM images of the internal morphology of PPZL, ZnO NPs, and LIG IDEs.

Figure 3a explores the influence of the gas sensor performance under different UV irradiations. The commercial LED patch we used has a maximum power of 0.5 W, and output power can be adjusted by modifying the input current (ranging from 0.26 to 26 mW/cm^2). As the light power increases, the device's initial resistance in air (R_a) first decreases and then slowly increases. This is due to the photovoltaic effect, where the energy density of light per unit area per unit time directly impacts the number of photons scattered per unit area per unit time. As light irradiation increases, the number of photons passing through the ZnO material surface also increases, consequently elevating the number of photoelectrons escaping from the material surface per unit time, thus reducing the steady-state initial resistance R_a. At 4.05 mW/cm^2, the photocurrent reaches saturation; further increases in light irradiation lead to an abundance of EHPs, reducing carrier lifetimes as their concentration increases, enhancing recombination effects, and causing a slow rise in R_a. In Figure 3b, response and recovery times for detecting 100 ppm of acetone vary with light irradiation. Response time decreases initially, then slightly rises, whereas recovery time drops quickly at first, then more gradually. The shortest total response and recovery times occur around a light irradiation of 4.05 mW/cm^2. Figure 3c shows how responsiveness (R_g/R_a) and R_a for 100 ppm of acetone change with light irradiation. R_a quickly drops and then slowly rises, while R_g/R_a sharply increases, then stabilizes after 4.05 mW/cm^2. The light irradiation of 4.05 mW/cm^2 is selected for optimal device performance, offering minimal response and recovery times and maximal sensitivity.

Figure 4 illustrates the acetone-gas-sensitive performance of the UV-assisted gas sensor under UV illumination at 4.05 mW/cm^2. Dynamic tests (Figure 4a) for acetone gas concentrations ranging from 1 to 100 ppm were conducted at room temperature. The device exhibited a 1 ppm response for acetone gas, and the theoretical limit of detection (LOD) can be calculated by

$$\mathrm{LOD} = 3 \times \frac{\mathrm{SE} \times \sqrt{N}}{\mathrm{slope}} \quad (5)$$

https://doi.org/10.1021/acsami.4c16209
ACS Appl. Mater. Interfaces 2024, 16, 62436−62445

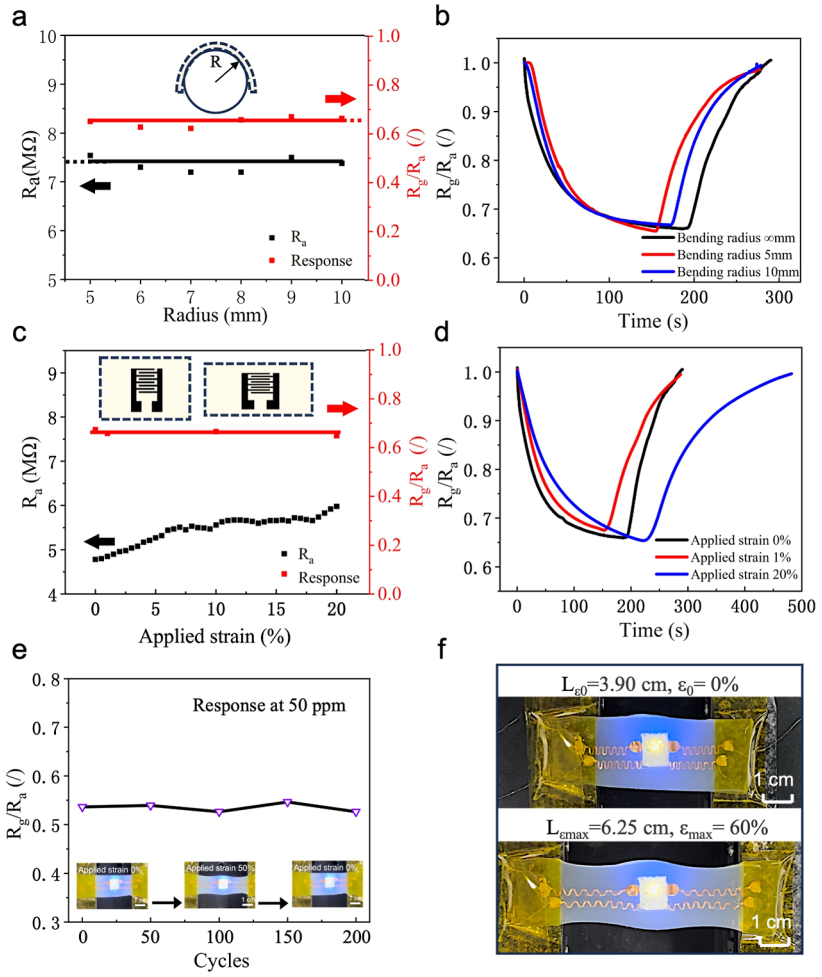

Figure 5. Flexibility and durability tests of the wearable acetone gas sensor. (a) R_a and response R_g/R_a under bending strains ranging from 5 to 10 mm. (b) Response and recovery times to 30 ppm acetone under varying bending strains. (c) R_a and response R_g/R_a under applied strains from 0% to 20%. (d) Response and recovery times to 30 ppm acetone under varying applied strains. (e) Long-term performance test of the sensor under maximum strain conditions. (f) Visual representation of the sensor's flexibility, showing the sensor's initial state (L_0 = 3.90 cm and ε_0 = 0%) and after maximum stretching (L_{max} = 6.25 cm and ε_{max} = 60%).

where N is the number of tests, SE is the standard error of intercept. And LOD is calculated to be ∼2.8 ppm. The gas sensor showed excellent linearity (Figure 4b) within the ranges of 1−100 ppm and 1−20 ppm, with a sensitivity of ∼0.9%/ppm. The response time of the sensor averagely ranged from 110 to 150 s, and the recovery time averagely ranged from 130 to 180 s across different acetone concentrations (Figure 4c). Notably, for 100 ppm of acetone, the response and recovery times were 110 and 100 s, respectively, while for 3 ppm of acetone, they were 135 and 180 s (Figure S14). Repetitive tests (Figure 4d) on the device demonstrated a stable original resistance baseline and consistent response, with R_g/R_a remaining stable during tests with 100 ppm of acetone gas, highlighting the performance benefits of UV assistance in reducing limit drift (Figure S15). A long-term stability test (Figure 4e) was performed on the device, evaluating its response over 20 days to 3, 5, and 50 ppm acetone concentrations, demonstrating good consistency and long-term stability.

The impacts of environmental humidity on sensor's electrical performance and acetone's chemical sensitivity were investigated, as shown in Figure S16. In low-humidity environments, water molecules chemically adsorb onto the surface of ZnO nanoparticles, occupying O_2^- adsorption sites, leading to hydroxyl poisoning and increased conductivity. In high-humidity environments, apart from the chemical adsorption of water molecules, a physical adsorbed water film forms on the surface, resulting in a phenomenon of physiochemical coadsorption, conductivity tends to saturate and no longer change.[33] Concurrently, we studied the response of 50 ppm of acetone under six RH conditions, revealing a consistent R_g/R_a value. Despite fewer adsorption sites in high RH due to hydroxyl positioning, resulting in decreased R_g, the proportional decrease in R_a maintains consistency in the R_g/R_a response to the same acetone concentration across RH levels (Figure 4f.).

2.3. Flexibility Test for PPZL and Wearable Sensors.

Figure 5 outlines the flexibility test for the PPZL and the wearable gas sensor. Using different bending radii imposed by cylinders and a displacement platform, as can be seen in Figure S17, PPZL's gas-sensing performance stability can be verified under various strains.

Figure 5a,b depicts PPZL strain tests at different bending radii (5−10 mm). The device's original resistance R_a showed fluctuations with bending strain but did not reach saturation within the tested range. Gas sensitivity tests for 30 ppm

https://doi.org/10.1021/acsami.4c16209
ACS Appl. Mater. Interfaces 2024, 16, 62436−62445

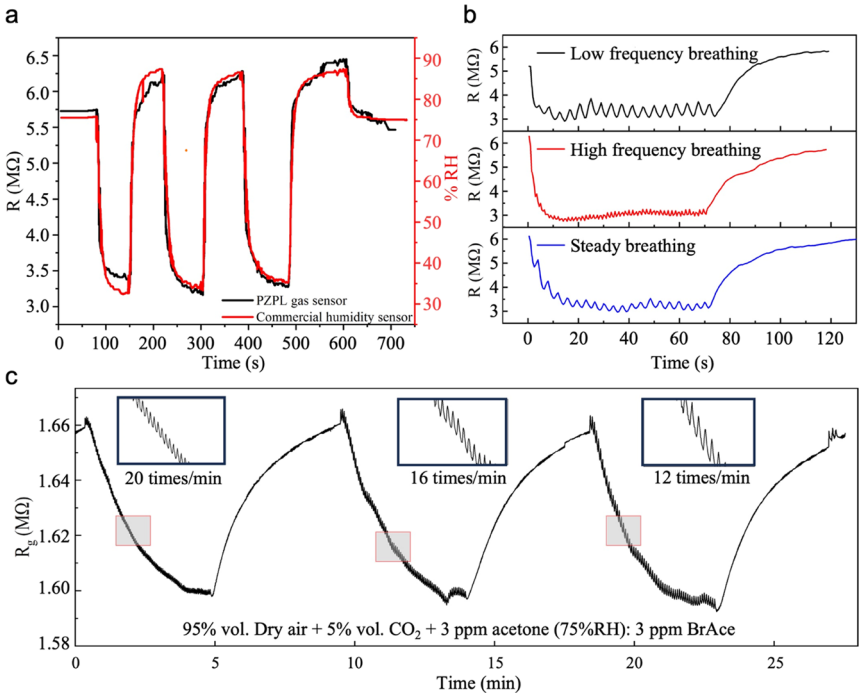

Figure 6. BrAce detection and breath event analysis. (a) Comparison of humidity-sensing performance between the PPZL gas sensor and a commercial humidity sensor. (b) Human wear tests for different breathing patterns (low-frequency breathing, high-frequency breathing, and steady breathing patterns). (c) Simulated test for detecting 3 ppm BrAce under three different breathing patterns. The insets highlight the sensor's response during different breathing events.

acetone at a bending radius of ∞, 5, and 10 mm demonstrated consistent R_g/R_a around 65%. Response and recovery times remained relatively unchanged. Figure 5c,d presents PPZL strain tests under various applied strains (0%−20%). The device's original resistance R_a increased with applied strain. Gas sensitivity tests for 30 ppm of acetone under different applied strains demonstrated consistent R_g/R_a around 65%, with the fastest response and recovery times at 0% strain, slowing as the strain increased to 20%. The findings show that the resistance R_a increases with strain due to the ZnO NPs interconnecting within the PDMS framework expanding, yet the surface redox reactions of ZnO remain unaffected, ensuring stable responses to the same concentration of acetone gas. This suggests that mechanical strain affects sensor dynamics by altering the volume of gas channels, impacting gas exchange.

Figure 5e,f describes the flexibility test of the wearable gas sensor. Figure 5e details a progressive stretching test on the sensor, captured via a phone video. Using ImageJ software to analyze the footage, the device was stretched from its original length (L_{ε_0} = 3.90 cm) to a maximum length ($L_{\varepsilon_{max}}$ = 6.25 cm), causing the LED to turn off due to the failure of the serpentine copper electrode structure, with the wearable room-temperature acetone gas sensor enduring a maximum strain of approximately 60%. Figure 5f uses a flexible electronics multimodal testing system to subject the sensor to cyclical stretching fatigue treatments ranging from 0% to 50% strain. After every 50 stretch cycles, the sensor was removed for a gas performance test with 50 ppm of acetone gas. Sensors subjected to 0, 50, 100, 150, and 200 stretching cycles consistently demonstrated consistent R_g/R_a when detecting 50 ppm acetone, proving that the wearable sensor retains good durability and gas sensitivity after the fatigue test.

Figure S18 features an experimental control device manufactured using the same process but without PPZL. This control group was used to characterize the UV LED layer's irradiation under stretching strain. The LED control group maintained consistent light irradiation and mechanical stability even when subjected to up to 60% applied strain, ensuring reliable performance in wearable applications.

2.4. Multifunctional Sensor System for Breath Detection and Analysis. This flexible room-temperature acetone gas sensor, capable of high-linearity acetone concentration tests even under stretch and strain, enables wearable testing of exhaled breath, as depicted in Figure 1b.

Figure 6a illustrates the humidity-sensing performance of the PPZL gas sensor compared with a commercial humidity sensor. The PPZL sensor demonstrates accurate monitoring of RH signals, with fast response and recovery times. In Figure 6b, breath event measurements were taken while the sensor was worn under the nose of a volunteer (24 year-old female). The sensor quickly reached a saturation resistance of the humidity of exhaled breath within 10 s and was able to accurately identify different breathing rates: 14 breaths per minute (low-frequency breathing), 33 breaths per minute (high-frequency breathing), and 17 breaths per minute (steady breathing), demonstrating its capability to accurately recognize breathing patterns.

Using a dynamic gas delivery platform (Figure S19) to simulate 3 ppm of BrAce (gas mixture: 95% vol dry air, 5% vol CO_2, and 3 ppm acetone at 75% RH), three breathing modes were set up. Figure 6c shows the results for simulated BrAce frequencies. For 3 ppm BrAce, the sensor was able to reach acetone signal saturation within 3 min after attaining humidity equilibrium (75% RH) with simulated exhaled breath. The insets highlight the sensor's response during different breathing events, indicating its ability to detect low concentrations of

https://doi.org/10.1021/acsami.4c16209
ACS Appl. Mater. Interfaces 2024, 16, 62436−62445

acetone in exhaled breath, which is critical for applications in diabetes monitoring. Across different breath frequencies, it maintained a similar response with an R_g/R_a ratio of ∼0.97.

3. CONCLUSIONS

In summary, we have developed a novel method for synthesizing a flexible, porous PDMS−ZnO composite with adjustable conductivity and porosity. This composite integrates stretchable LIG IDEs, combined with UV LED, serpentine copper electrodes, and a low-modulus Ecoflex frame structure to create a conformal, wearable, UV-assisted acetone gas sensor. Under 4.05 mW/cm^2 UV illumination, the sensor exhibits high sensitivity and rapid response within the 1−100 ppm acetone concentration range. Compared to other wearable gas sensors, it maintains stable gas-sensitive performance under stretch, bend, and fatigue conditions with a sensitivity of 0.9%/ppm. Both response and recovery times are under 3 min, demonstrating excellent repeatability and long-term stability.

Human trials with a compact circuit module based on the ESP32 C3 circuit for Bluetooth signal communication have confirmed the sensor's ability to identify different breathing patterns accurately. Tests for 3 ppm of BrAce simulations have shown the potential for detecting acetone exhalation across various breathing modes. This work lays the groundwork for noncontact multifunction breath detection and analysis. Furthermore, the method proposed for manufacturing the flexible PPZL composite opens new possibilities for the diversified design and application of flexible MOX semiconductor composite materials.

4. MATERIALS AND METHODS

4.1. Materials. All chemicals used in the experiments are of analytical reagent grade without further treatment. The water used in all of the experiments was DI water. PDMS elastomer kits (Sylgard 184) were purchased from Dow Corning (Midland, MI). ZnO NPs was purchased from Aladin Company. Ecoflex 00-20 was purchased from the Smooth-on Company. *n*-Hexane (for GC, ≥99.0% (GC)) was purchased from the Aladin Company.

4.2. Fabrication of a Gas Sensor. The conformal gas sensor comprises a gas-sensitive layer of PPZL integrated with LIG IDEs and a UV LED excitation layer. Figure S20 details the fabrication process of the wearable acetone gas sensor, highlighting the detailed steps for each layer and component:

1. Layer A (PPZL): The gas-sensing layer, crucial for detecting acetone gas and humidity, whose optimization is detailed in Section 1, with its fabrication and optimization process illustrated in Figure 2b.
2. Layer B (UV LED): Ecoflex A and B solutions were mixed in 1:1 mass ratio and applied to a clean silicon wafer at 700 rpm using a spin coater; The Ecoflex layer was cured at 80 °C for 30 min to form a 100 μm film and used as an adhesive medium for copper foil; 10 μm-thick copper foil was laminated to the Ecoflex layer and pattern precisely using a UV laser engraver (laser power: 3.5 W and laser speed: 90 mm/s) and then folded into a 3D spring structure; LEDs were attached to the copper electrodes using thermosetting silver paste and cured at 120 °C for 20 min; and the structure was covered with a PDMS precursor mixed with a curing agent at a 10:1 ratio and cured at 80 °C for 30 min to encapsulate the UV LED layer.
3. Serpentine electrode connection and encapsulation: The serpentine copper electrodes connecting the LED layer and PPZL were transferred to an external Ecoflex layer and secured with water-soluble PVA tape, and then the electrode pads were soldered. The geometric structure design of the serpentine copper electrode can be seen in Figure S21.[34]
4. Assembly of PPZL and UV LED layers: Using the oxygen plasma bonding method, the PDMS surfaces of both layers were treated for 2 min to create hydrogen bonding sites. The layers were aligned and pressed together and then cured at 80 °C for 30 min to bond, forming a complete sensor unit.
5. External encapsulation: The sensor was encapsulated externally with Ecoflex to protect it, completing the preparation of the wearable sensing system.

The above steps successfully fabricated a flexible acetone gas sensor with a high sensitivity and good stability.

The LIG material was chosen for fabricating IDEs due to its ease of manufacture and patternability, and its 3D porous fibrous structure significantly increases the surface area at the contact interface, enhancing the interfacial contact energy. Moreover, as a flexible gas sensor material, LIG maintains its conductivity under some degree of stretching due to its excellent elasticity and flexibility.

LIG was prepared on a PI film by using a 10.6 μm CO_2 infrared laser. The effects of laser energy density E_d[35] on LIG performance are detailed in Figure S22, and a laser power parameter of 3.6 W and 90 mm/s with a fibrous morphology was chosen for manufacturing, as lateral fiber overlapping enhances strain resistance capabilities (Figure S23). The microstructure of LIG was modified using oxygen plasma etching and low-temperature annealing processes (Figure S24), ultimately producing a fractal fiber structure LIG (Figure S25) with improved permeability and enhanced peel integrity (Figure S26), enhancing its strain resistance from a gauge factor of 14−7 (Figure S27).

4.3. Characterizations. ZnO NP samples were observed using a UV−Vis spectrophotometer (Shimadsu UV-3600). The surface morphology and microstructure of the samples were studied using field emission scanning electron microscopy (FESEM; JEOL JSM-7600F) and CT. The output resistance was recorded by a digital multimeter (34470 A, KEYSIGHT). The degree of graphitization in the LIG material of IDEs was accessed by using Raman analysis. The C 1s peak of the LIG material was examined by using XPS analysis.

Figure S17a illustrates the gas dynamic testing platform, confirming its accuracy. We established a gas sensor testing platform to evaluate the resistive gas sensor detailed in this study. This platform includes various gas sources, pipelines, mass flow controllers (MFCs), gas chambers, and data acquisition and analysis systems. It uses 100 ppm standard acetone gas (Huatepeng Company) and is diluted in dry air (21% O_2 and 79% N_2) mixed with 5% dry CO_2 gas to achieve the desired concentration and monitor the human exhaled breath. Various pipelines introduce different gases into the chamber, controlled by MFCs to regulate flow rates between the target and carrier gases. The gases mix thoroughly before entering the chamber, made from polytetrafluoroethylene (Teflon), chosen for its mechanical strength, thermal stability, chemical inertness, and minimal gas adsorption. The platform operates at room temperature, continuously feeding test gas at a stable rate, ensuring a consistent target gas molecule concentration within the atmosphere.

Figure S17b,c shows that dynamic mixtures with 20, 40, and 60 ppm acetone were prepared and stored in Tedlar bags. Mass spectrometry confirmed the system's linearity and accuracy in configuring gas concentrations.

■ ASSOCIATED CONTENT

Supporting Information

The Supporting Information is available free of charge at https://pubs.acs.org/doi/10.1021/acsami.4c16209.

Comparative performance of ZnO-based sensing materials for acetone detection; UV−vis absorption spectroscopy of ZnO NPs; gas sensor circuit; dynamic acetone response under UV light; SEM, tensile testing, strain simulation, and porosity optimization of PPZL; electrical and gas-sensing performance with process optimizations; acetone permeability and surface morphologies; dynamic response, stability, and testing under strain; gas

https://doi.org/10.1021/acsami.4c16209
ACS Appl. Mater. Interfaces 2024, 16, 62436−62445

distribution system and validation; fabrication of gas sensor and serpentine copper electrode; and LIG IDE fabrication and strain performance enhancement (PDF)

AUTHOR INFORMATION

Corresponding Author

Min Zhang − *Shenzhen Intern ational Graduate School, Tsinghua University, Shenzhen 518055, China;* orcid.org/0000-0003-2219-8030; Email: zhang.min@sz.tsinghua.edu.cn

Authors

Yanru Chen − *Shenzhen Intern ational Graduate School, Tsinghua University, Shenzhen 518055, China*

Yixin Liu − *Shenzhen Intern ational Graduate School, Tsinghua University, Shenzhen 518055, China;* orcid.org/0000-0002-9190-3736

Jiaqi Liu − *Shenzhen Intern ational Graduate School, Tsinghua University, Shenzhen 518055, China*

Yuzhen Li − *Shenzhen Intern ational Graduate School, Tsinghua University, Shenzhen 518055, China*

Yuhan Liu − *Shenzhen Intern ational Graduate School, Tsinghua University, Shenzhen 518055, China*

Wenjie Zhang − *Shenzhen Intern ational Graduate School, Tsinghua University, Shenzhen 518055, China*

Liuyang Han − *Shenzhen Intern ational Graduate School, Tsinghua University, Shenzhen 518055, China*

Dongkai Wang − *Shenzhen Intern ational Graduate School, Tsinghua University, Shenzhen 518055, China*

Shuhong Cao − *Shenzhen Intern ational Graduate School, Tsinghua University, Shenzhen 518055, China*

Hanxiao Liu − *Shenzhen Intern ational Graduate School, Tsinghua University, Shenzhen 518055, China*

Qisen Xie − *Shenzhen Intern ational Graduate School, Tsinghua University, Shenzhen 518055, China*

Xiaohao Wang − *Shenzhen Intern ational Graduate School, Tsinghua University, Shenzhen 518055, China*

Complete contact information is available at: https://pubs.acs.org/10.1021/acsami.4c16209

Notes

The authors declare no competing financial interest.

ACKNOWLEDGMENTS

This work was supported by the Shenzhen Fundamental Research Funds (No. JCYJ20220530143011026).

REFERENCES

(1) Mao, W.; Yip, C.-M. W.; Chen, W. Complications of Diabetes in China: Health System and Economic Implications. *BMC Public Health* **2019**, *19* (1), 269.

(2) Ramsing, B. China's Changing Diet: Environment and Health Impacts. *Center for a Livable Future*, 2024. https://clf.jhsph.edu/stories/chinas-changing-diet-environment-and-health-impacts.

(3) Sun, Y.; Dong, D.; Ding, Y. The Impact of Dietary Knowledge on Health: Evidence from the China Health and Nutrition Survey. *Int. J. Environ. Res. Public Health* **2021**, *18* (7), 3736.

(4) Gunji, S.; Jukei, M.; Shimotsuma, Y.; Miura, K.; Suematsu, K.; Watanabe, K.; Shimanoe, K. Unexpected Gas Sensing Properties of SiO_2/SnO_2 Core−Shell Nanofibers under Dry and Humid Conditions. *J. Mater. Chem. C* **2017**, *5* (25), 6369−6376.

(5) Benjafield, A. V.; Ayas, N. T.; Eastwood, P. R.; Heinzer, R.; Ip, M. S. M.; Morrell, M. J.; Nunez, C. M.; Patel, S. R.; Penzel, T.; Pépin, J. L.; Peppard, P. E.; Sinha, S.; Tufik, S.; Valentine, K.; Malhotra, A. Estimation of the Global Prevalence and Burden of Obstructive Sleep Apnoea: A Literature-Based Analysis. *Lancet Respir. Med.* **2019**, *7* (8), 687−698.

(6) Adiguzel, Y.; Kulah, H. Breath Sensors for Lung Cancer Diagnosis. *Biosens. Bioelectron.* **2015**, *65*, 121−138.

(7) Wang, Z.; Wang, C. Is Breath Acetone a Biomarker of Diabetes? A Historical Review on Breath Acetone Measurements. *J. Breath Res.* **2013**, *7* (3), 037109.

(8) Li, W.; Liu, Y.; Lu, X.; Huang, Y.; Liu, Y.; Cheng, S.; Duan, Y. A Cross-Sectional Study of Breath Acetone Based on Diabetic Metabolic Disorders. *J. Breath Res.* **2015**, *9* (1), 016005.

(9) Wang, C.; Mbi, A.; Shepherd, M. A Study on Breath Acetone in Diabetic Patients Using a Cavity Ringdown Breath Analyzer: Exploring Correlations of Breath Acetone With Blood Glucose and Glycohemoglobin A1C. *IEEE Sensors J.* **2010**, *10* (1), 54−63.

(10) Saasa, V.; Beukes, M.; Lemmer, Y.; Mwakikunga, B. Blood Ketone Bodies and Breath Acetone Analysis and Their Correlations in Type 2 Diabetes Mellitus. *Diagnostics* **2019**, *9* (4), 224.

(11) Maier, D.; Laubender, E.; Basavanna, A.; Schumann, S.; Güder, F.; Urban, G. A.; Dincer, C. Toward Continuous Monitoring of Breath Biochemistry: A Paper-Based Wearable Sensor for Real-Time Hydrogen Peroxide Measurement in Simulated Breath. *ACS Sens.* **2019**, *4* (11), 2945−2951.

(12) Zhong, J.; Li, Z.; Takakuwa, M.; Inoue, D.; Hashizume, D.; Jiang, Z.; Shi, Y.; Ou, L.; Nayeem, M. O. G.; Umezu, S.; Fukuda, K.; Someya, T. Smart Face Mask Based on an Ultrathin Pressure Sensor for Wireless Monitoring of Breath Conditions. *Adv. Mater.* **2022**, *34* (6), 2107758.

(13) Lin, Q.; Zhang, F.; Zhao, N.; Zhao, L.; Wang, Z.; Yang, P.; Lu, D.; Dong, T.; Jiang, Z. A Flexible and Wearable Nylon Fiber Sensor Modified by Reduced Graphene Oxide and ZnO Quantum Dots for Wide-Range NO2 Gas Detection at Room Temperature. *Materials* **2022**, *15* (11), 3772.

(14) Zhang, Y.; Jia, C.; Kong, Q.; Fan, N.; Chen, G.; Guan, H.; Dong, C. ZnO-Decorated In/Ga Oxide Nanotubes Derived from Bimetallic In/Ga MOFs for Fast Acetone Detection with High Sensitivity and Selectivity. *ACS Appl. Mater. Interfaces* **2020**, *12* (23), 26161−26169.

(15) Ahmadipour, M.; Pang, A. L.; Ardani, M. R.; Pung, S.-Y.; Ooi, P. C.; Hamzah, A. A.; Mohd Razip Wee, M. F.; Aniq Shazni Mohammad Haniff, M.; Dee, C. F.; Mahmoudi, E.; Arsad, A.; Ahmad, M. Z.; Pal, U.; Chahrour, K. M.; Haddadi, S. A. Detection of Breath Acetone by Semiconductor Metal Oxide Nanostructures-Based Gas Sensors: A Review. *Mater. Sci. Semicond. Process.* **2022**, *149*, 106897.

(16) Ramola, R. C.; Negi, S.; Rawat, M.; Singh, R. C.; Singh, F. Annealing Effects on Gas Sensing Response of Ga-Doped ZnO Thin Films. *ACS Omega* **2021**, *6* (17), 11660−11668.

(17) Abbas Shah, N.; Gul, M.; Abbas, M.; Amin, M. Synthesis of Metal Oxide Semiconductor Nanostructures for Gas Sensors. In *Gas Sensors*; Bahadar Khan, S., Asiri, A. M., Akhtar, K., Eds.; IntechOpen, 2020.

(18) Chaudhary, S.; Umar, A.; Bhasin, K.; Baskoutas, S. Chemical Sensing Applications of ZnO Nanomaterials. *Materials* **2018**, *11* (2), 287.

(19) Zhang, H.; Liu, L.; Huang, C.; Liang, S.; Jiang, G. Enhanced Acetone Gas Sensing Performance of ZnO Polyhedrons Decorated with $LaFeO_3$ Nanoparticles. *Mater. Res. Express* **2023**, *10* (9), 095902.

(20) Lee, G.; Sim, J.-H.; Oh, G.; Won, M.; Mantry, S. P.; Kim, D.-S. Electrostatic Spray Deposition of Al-Doped ZnO Thin Films for Acetone Gas Detection. *Processes* **2023**, *11* (12), 3390.

(21) Wang, H.; Wang, D.; Tian, L.; Li, H.; Wang, P.; Ou, N.; Wang, X.; Yang, J. Graphene-Like Porous ZnO/Graphene Oxide Nanosheets for High-Performance Acetone Vapor Detection. *Molecules* **2019**, *24* (3), 522.

(22) Saber, G.; El-Dissouky, A.; Badie, G.; Ebrahim, S.; Shokry, A. Capped ZnO Quantum Dots with a Tunable Photoluminescence for Acetone Detection. *RSC Adv.* **2023**, *13* (24), 16453−16470.

(23) Jaisutti, R.; Lee, M.; Kim, J.; Choi, S.; Ha, T.-J.; Kim, J.; Kim, H.; Park, S. K.; Kim, Y.-H. Ultrasensitive Room-Temperature Operable Gas Sensors Using p-Type Na:ZnO Nanoflowers for Diabetes Detection. *ACS Appl. Mater. Interfaces* **2017**, *9* (10), 8796−8804.
(24) Zhang, L.; Hao Guo, Y. Y.; Liu, G.; Tan, Q. Na-Doped ZnO and RGO Composite-Based Flexible Acetone Gas Sensor Operated in Room Temperature. *IEEE Access* **2020**, *8*, 171568−171574.
(25) Deng, C.; Zhang, J.; Yu, X.; Zhang, W.; Zhang, X. Determination of Acetone in Human Breath by Gas Chromatography−Mass Spectrometry and Solid-Phase Microextraction with on-Fiber Derivatization. *J. Chromatogr. B* **2004**, *810* (2), 269−275.
(26) Turner, C.; Walton, C.; Hoashi, S.; Evans, M. Breath Acetone Concentration Decreases with Blood Glucose Concentration in Type I Diabetes Mellitus Patients during Hypoglycaemic Clamps. *J. Breath Res.* **2009**, *3* (4), 046004.
(27) Khorsand Zak, A.; Abd Majid, W. H.; Abrishami, M. E.; Yousefi, R. X-Ray Analysis of ZnO Nanoparticles by Williamson−Hall and Size−Strain Plot Methods. *Solid State Sci.* **2011**, *13* (1), 251−256.
(28) Raza, M. H.; Kaur, N.; Comini, E.; Pinna, N. SnO_2-SiO_2 1D Core-Shell Nanowires Heterostructures for Selective Hydrogen Sensing. *Adv. Mater. Interface* **2021**, *8* (17), 2100939.
(29) Wu, Y.; Karakurt, I.; Beker, L.; Kubota, Y.; Xu, R.; Ho, K. Y.; Zhao, S.; Zhong, J.; Zhang, M.; Wang, X.; Lin, L. Piezoresistive Stretchable Strain Sensors with Human Machine Interface Demonstrations. *Sens. Actuators, A* **2018**, *279*, 46−52.
(30) Brigandi, P. J.; Cogen, J. M.; Pearson, R. A. Electrically Conductive Multiphase Polymer Blend Carbon-Based Composites. *Polym. Eng. Sci.* **2014**, *54* (1), 1−16.
(31) Smith, A. M.; Inocencio, D. G.; Pardi, B. M.; Gopinath, A.; Andresen Eguiluz, R. C. Facile Determination of the Poisson's Ratio and Young's Modulus of Polyacrylamide Gels and Polydimethylsiloxane. *ACS Appl. Polym. Mater.* **2024**, *6* (4), 2405−2416.
(32) Panalytical, M. *Controlling Rheology by Changing the Size, Zeta Potential and Shape of Particles*; AZoM, 2024. https://www.azom.com/article.aspx?ArticleID=5542. (accessed March 16, 2024).
(33) Kannan, P. K.; Saraswathi, R.; Rayappan, J. B. B. A Highly Sensitive Humidity Sensor Based on DC Reactive Magnetron Sputtered Zinc Oxide Thin Film. *Sens. Actuators, A* **2010**, *164* (1−2), 8−14.
(34) Rogers, J.; Ghaffari, R.; Kim, D.-H. *Stretchable Bioelectronics for Medical Devices and Systems*; Springer, 2016.
(35) Liu, Y.; Li, H.; Zhang, M. Wireless Battery-Free Broad-Band Sensor for Wearable Multiple Physiological Measurement. *ACS Appl. Electron. Mater.* **2021**, *3* (4), 1681−1690.

https://doi.org/10.1021/acsami.4c16209
ACS Appl. Mater. Interfaces 2024, 16, 62436−62445